

Measurement of Stenosis from Magnetic Resonance Angiography Using Vessel Skeletons

Peter J. Yim^{*}, Rakesh Mullick^{*}, Ronald M. Summers^{*}, Hani Marcos^{*},
Juan R. Cebal[•], Rainald Lohner[•], Peter L. Choyke^{*}

^{*}Diagnostic Radiology Department, National Institutes of Health, Bethesda, MD. 20892

[•]Institute for Computational Sciences and Informatics,
George Mason University, Fairfax, VA 22030

ABSTRACT

Measurement of stenosis due to atherosclerosis is essential for interventional planning. Currently, measurement of stenosis from magnetic resonance angiography (MRA) is made based on 2D maximum intensity projection (MIP) images. This methodology, however, is subjective and does not take full advantage of the 3D nature of MRA. To address these limitations we present a deformable model for reconstructing the vessel surface with particular application to the carotid artery.

The deformable model is based on a cylindrical coordinate system of a curvilinear axes. In this coordinate system, the location of each point on the surface of the deformable model is described by its axial, circumferential and radial position. The points on the surface deform in the radial direction so as to minimize discontinuity in radial position between adjacent points while maximizing the proximity of the surface to local edges in the image. The algorithm has no bias towards either narrower or wider cross-sectional shapes and is thus appropriate for the measurement of stenosis. Axes of the vessels are indicated manually or determined by axes detection methods. Once completed, the surface reconstruction lends itself directly to 3D methods for measuring cross-sectional diameter and area.

Keywords: Atherosclerosis, Carotid Artery, Stenosis, Magnetic Resonance Angiography, Surface Reconstruction, Deformable Model, Surface Merging, Skeletonization

1. INTRODUCTION

Measurement of carotid artery shape is important for clinical evaluation of atherosclerosis and for experimental studies of carotid artery hemodynamics. Stenosis, or narrowing of the vessel lumen, of the internal carotid artery is directly associated with risk of stroke. The NASCET¹ found that patients with greater than 70% stenosis respectively should be referred for endarterectomy or surgical removal of the carotid plaque. Furthermore, measurement of stenosis by magnetic resonance angiography (MRA) correlates with measurements by quantitative x-ray angiography while avoiding the risks associated with x-ray angiography². A more detailed description of shape is also useful for computational modeling of the hemodynamics which may allow for diagnostic assessment of mechanical properties of the vessel wall and lead to insights into the disease process of atherosclerosis^{3,4,5}.

In this paper, we will present new methodologies for reconstructing the surface of the carotid artery from Gadolinium (Gd) contrast-enhanced MRA and for characterizing the shape of the carotid artery. The methods include a semi-automated deformable model for vessel surface reconstruction, a method for joining two surfaces which is necessary at vessel bifurcations and a method for computational measurement of vessel size in 3D. We will review related work in the next section. We will then present our methodologies in sections 3-5. We will conclude with validation studies carried out on a digital phantom and on patient data in sections 6 and 7.

2. Background

The primary problem which we address is the reconstruction of the surface of blood vessels. Reconstruction of blood vessels is a challenging problem due to imaging artifacts which include those related to flow, magnetic field inhomogeneity, imperfect timing of the arrival of the contrast agent, and the partial-volume effect. Image noise is also considerable and image resolution is low relative to the vessel diameter. Moreover, normal and pathologic vessel geometry is complex and therefore, *a priori* knowledge of shape cannot be readily applied to the surface reconstruction. However, a variety of approaches have been taken to solving the problem of reconstructing the surface of the vessels from MRA.

The most straightforward method of surface reconstruction of MRA is the isosurface method in which all vertices on the surface share the same interpolated intensity value⁶. This methodology may also be combined with connectivity criteria to distinguish vessels from surrounding high-intensity non-vascular tissue. However, the iso-intensity value must be chosen by trial-and-error and a single iso-intensity value may not be valid for the entire vessel or vessel tree.

Several segmentation methods have been developed for blood vessels that objectively determine which voxels are inside and outside of the vessels. Segmentation locates the surface only within the resolution of the image but is an important first step in the surface reconstruction.

A clustering method has been developed for brain MRA which incorporates the principle of K-means clustering in which optimal thresholds are chosen to classify an image into a given number of tissue types. In this method, segmentation by the clustering threshold is modified by connectivity information. However, a validation study showed the method to be only moderately reliable⁷.

The fuzzy connectivity approach has also been applied to the analysis of MRA. This method extends the conventional region-growing method by assigning fuzzy membership to all points in the image rather than the binary Inside-Outside classification of conventional region growing. Tissue classes are identified by placing seed points at various points inside and outside of the vessels. The method has been found to be useful in the visualization of MRA using intra-vascular contrast where artery-vein overlap is considerable⁸. The method has not been tested, to our knowledge, on other types of MRA where tissue classes are less well defined.

The marker controlled watershed segmentation method has been applied to a high-resolution CT image of the pulmonary arteries and a contrast-enhanced MRA of the thoracic aorta^{9,10}. Boundaries of the marker-controlled watershed fall along the ridges in the intensity surface of the gradient magnitude image. The precise location of the watershed boundary is largely independent of the placement of the markers that indicate the interior and exterior of the vessel. Furthermore, smooth surfaces can be reconstructed from the watershed segmentation without resort to surface smoothing operations. However, image intensity within the carotid artery in Gd contrast-enhanced MRA may be highly inhomogeneous due to wide variation in flow rate. Due to that problem, the watershed segmentation is prone to large errors in vessels such as the carotid artery.

Another class of methods for surface reconstruction are those which are based not only on image -intensity information but also on geometrical constraints or *a priori* knowledge of shape. Adaptive deformable models have been applied to MRA and CTA which impose smoothing constraints on the surface but allow for protrusions in the shape which includes vessel branches and aneurysms^{11,12}. One method¹² was found to truncate vessels whose diameter is small and may be ineffective in larger vessels with stenosis. The method was also found to produce inaccuracies near bifurcations due to geometric complexities.

Promising results have been obtained from methods that are specific to angiography analysis^{13,14}. In these methods, the surface reconstruction begins by determination of the axis of the vessels by ridge tracking methods. The surface is found by determining the radii associated with each point along the vessel axis

using estimates of scale. Radius-based surfaces can be used as initializations for a mechanical-analog deformable model. This method however is highly dependent on the initialization of the vessel radii that may prove to be a problem with further testing.

3. The Deformable Model

3.1 The Cylindrical Deformation Process

We present a deformable model for blood vessels such as the carotid artery. The model we present allows for curves in the vessel axis, variability in the vessel diameter and variability in cross-sectional shape. The deformable model is a surface mesh which deforms towards points of high image-gradient intensity while maintaining smoothness of the surface. Our deformable model is based on a coordinate system which is cylindrical in nature. The vertices of the mesh are evenly spaced in the axial and circumferential directions and are connected with one another if they are adjacent in the axial or circumferential directions. In contrast to a previous deformable model of blood vessels¹⁴, the vertices deform only in the radial direction and their position is described only by their radial location. This formulation of the deformation process eliminates bias towards forming tubes of smaller diameter. Specifics of this cylindrical coordinate system will be discussed in the next section.

The surface reconstruction process is straightforward. First the location of each vertex is initialized to be the point along its radial path where the maximum of the gradient magnitude occurs provided the gradient at that point has roughly the same direction as the radial line. (a, ϕ, r) is the cylindrical coordinate of a vertex. I is the image intensity. \bar{D}_r is the direction of a given radial line at a given location. The radial location $r: \mathbf{R}^2 \rightarrow \mathbf{R}$ of a vertex is a function of the axial and circumferential positions.

$$\| \nabla I(a, \mathbf{j}, r_0(a, \mathbf{j})) \| \geq \| \nabla I(a, \mathbf{j}, r(a, \mathbf{j})) \| \quad (1)$$

for all $r(a, \phi)$ provided that

$$\bar{D}_r(a, \mathbf{j}, r(a, \mathbf{j})) \bullet \nabla I(a, \mathbf{j}, r(a, \mathbf{j})) > 0 \quad (2)$$

The vertices then deform so as to minimize discontinuities in the vertex radial position along the surface while maximizing the proximity of the vertices to edges in the image. This is obtained an equilibration process analogous to that of a mechanical system acted on by internal elastic forces and external forces. The motion of a vertex at any given moment in the course of the equilibration is given by

$$\Delta r_n(a, \mathbf{j}) = K_1(K_2 \sum_i \Delta r_i(a, \mathbf{j}) - \bar{D}(a, \mathbf{j}) \bullet \nabla \| \nabla I(a, \mathbf{j}, r(a, \mathbf{j})) \|) \quad (3)$$

where Δr_i is the difference in radial location between a given vertex and that of each of its axial and circumferential neighbors. $\nabla I(a, \mathbf{j}, r(a, \mathbf{j}))$ is the gradient operator implemented as the convolution of the image with a kernel which is the gradient of the normalized 3D gaussian function whose space constant is 1 voxel unit. The first term is the elastic force and the second term is the external force that pushes the vertices toward the peaks in the gradient magnitude image. This process is illustrated in figure 1. Within the cylindrical coordinate system, there is no bias towards forming smaller-diameter tubes. The elastic forces in this model pull the surface towards a tubular shape with a uniform radius that is centered at the axis but no radius is preferred.

K_1 is chosen to be sufficiently small to ensure that the system converges uniformly towards the equilibrium state. The choice of K_2 is made by trial-and-error for the patient data but a single value was found to apply well to all patient data.

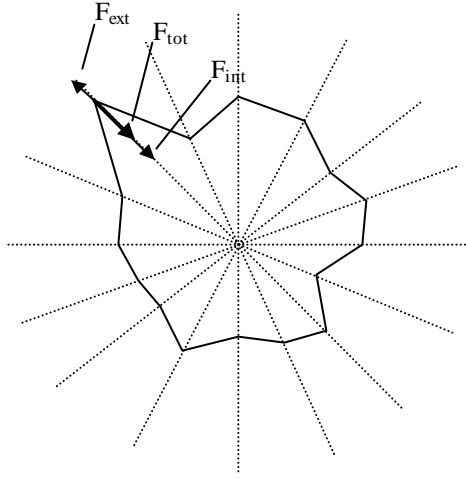


Figure 1. Deformation of vertices in a cylindrical coordinate system (only in-plane vertices shown). Deformation is produced by internal and external forces. The internal forces push the vertices to minimize discontinuities in the radial location between adjacent vertices while the external forces push the vertices towards peaks in the gradient-magnitude image. The dotted lines indicate radial lines. The polygonal figure is the in-plane section of the surface mesh. F_{ext} , F_{int} , and F_{tot} are the external, internal and total force respectively on the vertex.

3.2 The Modified Cylindrical Coordinate System

The deformable model of the vessels is based on a modified cylindrical coordinate system (MCCS) which allows for curvature of the cylindrical axis. Like the conventional cylindrical coordinate system, the location of all points in space can be described with the axial, circumferential and radial coordinates. However, several modifications must be made to accommodate curvature of the vessel axis.

The first modification is that the reference orientation for the cylindrical coordinate angle must change along the axis so as to remain normal to the vessel axis. We define a circumferential reference orientation in which minimum of change occurs from one point along the axis to the next. Let $\overline{D}_a(m)$ be the direction of the vessel axis at the m^{th} point, $\overline{D}_r(m,0)$ be the reference orientation at the m^{th} axial point and 0^{th} circumferential point. The reference orientation at the adjacent point is then:

$$\overline{D}_r(m+1,0,0) = \overline{D}_r(m,0,0) - \frac{\overline{D}_a(m+1) \cdot \overline{D}_a(m)}{\|\overline{D}_a(m)\| \|\overline{D}_a(m)\|} \quad (4)$$

The reference circumferential orientation for a curved axis is shown in figure 2.

A second feature of the MCCS is that the radii do not emanate in straight lines from the axis at all points. Rather, the radial lines may be warped in areas where the vessel axis is curved. This warping prevents radial lines emanating from adjacent axial locations from intersecting one another as is shown in figure 3. Should such intersections occur, certain locations would not have a unique set of coordinates.

We create a warping of the radial lines to avoid the intersection problem based on a merging mechanism. The radial lines are initially evenly spaced along the vessel axis and at equal angular spacing around the vessel axis and are oriented normal to the vessel axis. The initial unit radial vectors is in the direction given by (4).

The radial lines are then extended outwards at a step size, RADIAL_INCREMENT, of $\frac{1}{2}$ of the in-plane pixel resolution. Ideally, the radial lines should represent the shortest path from any point to the vessel axis. When this is not true, it is evidence of the condition where intersections between radial lines will occur. Thus, as the radial lines are being extended outwards, each of the radial lines is checked at each step to see if the origin of that particular radial line, $r(i, j, 0)$, is the closest of all the discrete locations along the vessel axis. If not, the radial line is considered terminated at that point and is not extended further along its original direction.

If the distance from $(a_i, \phi_j, r_k(a, \phi))$ to the axis is less than $k * \text{RADIAL_INCREMENT}$, then that particular radial line is terminated at the previous step, $k_{\max}(i, j) = k-1$.

Once the radial lines have been fully extended to $k = k_{\text{limit}}$, the terminated lines are extended by merging them with the closest radial lines that have not been terminated. In pseudo-code:

```

For  $k = k_{\text{limit}} - 1$  to  $k = 0$ 
  For all  $i$  and  $j$ , if  $k_{\max}(i, j) = k$  {
     $k_{\max}(i, j) = k_{\text{limit}}$ 
    For  $k' = k+1$  to  $k' = k_{\text{limit}}$ 
       $r_{k+1}(a_i, \phi_j, k+1) = r_{k+1}(a_{i, \text{nearest}}, \phi_j, k+1)$  }

```

Where $k_{\max}(i_{\text{nearest}}, j) = k_{\text{limit}}$.

Mesheres constructed from vertices at constant radial locations for a curved axis are shown in figure 4.

3.3 Merging Vertices

The cylindrical deformation process could be applied directly to the modified cylindrical coordinate system. However, bunching of vertices will occur where radial lines merge. Where such bunching occurs, the effective elasticity of the surface become significantly greater which reduces the surface smoothness. This effect is removed by merging vertices in the deformation process to match the merging of the radial lines. This precludes two vertices from co-existing on the same radial line. The procedure for merging vertices is as follows. The vertices initially exist for all circumferential and axial locations. After a primary deformation phase (200 iterations), vertices are merged with their axial neighbors if either of the vertices is at a point where the radial lines of the two vertices are merged. The radial location of the resulting vertex becomes the average of the locations of the vertices from which it was formed. Henceforth this vertex deforms as a single vertex. The neighbors of this resultant vertex are those of the merged vertices. However, the circumferential neighbors for the resultant vertex will accumulate relative to the axial neighbors. Therefore, to maintain a balance between the axial and circumferential component of the elastic force, the total circumferential elastic force must be rescaled. With regard to the equation of motion (equation 3) the elastic component Δr_i , the difference of radial location between a vertex and its neighbors, must be modified so that the circumferential and axial radial differences are added separately.

$$\Delta r_i(a, \mathbf{j}) = \sum_j \Delta_j r(a, \mathbf{j}) + \frac{2}{N} \sum_k \Delta_k r(a, \mathbf{j}) \quad (5)$$

where N is the number of circumferential neighbors of a merged vertex.

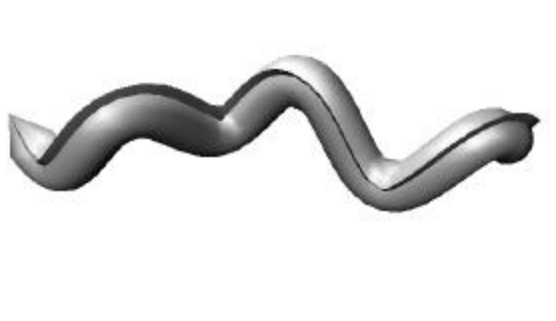


Figure 2. Reference orientation for circumferential coordinate angle. The reference angle on which the circumferential angle is based is dependent on the curvature of the vessel axis.

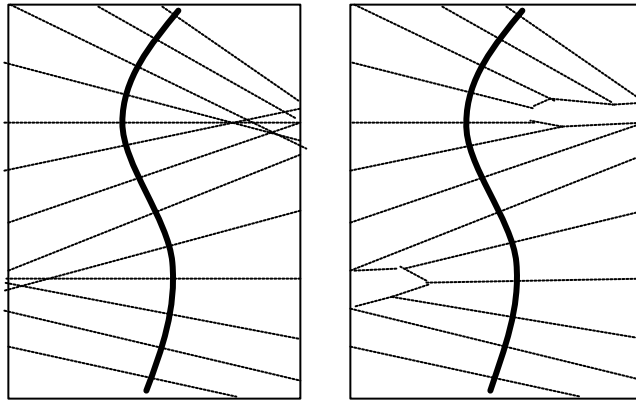
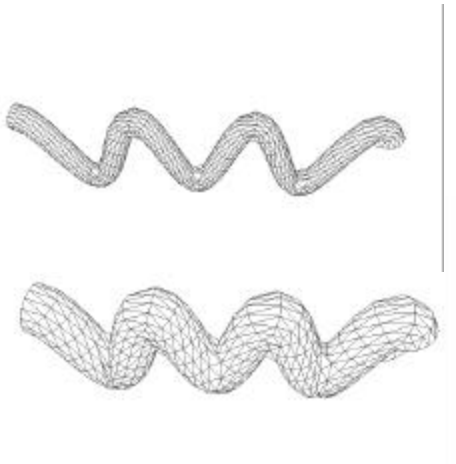


Figure 3. The modified cylindrical coordinate system (MCCS). A cylindrical coordinate system cannot be constructed from a curved axis using radii which are strictly normal to the axis. The problem with that coordinate system is shown on the left. For any given point, there will not be a unique axial and radial coordinate due to intersection of the radial lines. This problem is solved by merging radial lines in the MCCS (right). The radial coordinate at each point in the MCCS is the distance to the nearest point on the



axis.

Figure 4. Isodistance surfaces. Surfaces are constructed whose vertices are at equal distances from the given axis. The meshing is done according to the modified cylindrical coordinate system (MCCS). For small radii in the MCCS (top), vertices exist for each circumferential and axial position. At larger radii, the vertices merge with one another in the axial direction to eliminate criss-crossing of radial lines.



3.4 Formation of vessel axis

The primary method of user interaction is the initialization of the deformable model by indicating points along the axis of the vessel. We found that the vessel axis could be easily and reliably determined by picking points on axial views of the images with side-by-side view of an isosurface piercing the slice to provide context. This method is shown in figure 5. Points were indicated at every 5-20 slices along the vessel axis.

The spacing of points on the axis was increased to match the resolution of the image. We interpolated between each of the points specified by the user so as to describe the vessel axis as a contiguous path of voxels from one end of the vessel to the other. We then smoothed the path using a 10th order B-spline.

3.5 Anchor points

In some cases it is also desirable to also indicate specific known boundary locations. This is readily included within the mechanism of the deformable model. For a given point indicated by the user, the closest vertex of the deformable model is anchored at that location during the mechanical deformation. As a result, the surface will be pulled towards that location. Since the elasticity of the model is relatively low, for the anchor point to produce enough influence, the neighboring vertices (within 2 axial or circumferential positions) were also fixed at the same radial value as the anchor point.

4. Results

Good results for surface reconstruction have been obtained in contrast-enhanced MRA images (Intra-venous injection of Gd-DTPA, Spoiled Gradient Recalled Echo sequence, 256x224 matrix, 2mm thick slices, 0.5 NEX, in-in-plane sinc interpolation to 512x512 and 2X out of plane sinc interpolation, 35x35cm field of view) of 8 carotid arteries from 5 subjects (2 vessels were omitted because segment of vessel was missing due to extreme stenosis and 1 vessel was omitted due to severe image artifacts). We deform the model in 200 iterations prior to merging the vertices and 200 iterations after merging of the vertices. We use a value of 0.05 cm for the iteration step size (K_1) and a value of $2 \times 10^4 \text{ cm}^{-1}$ for the elasticity constant (K_2). The image intensities are in the range of 0 to about 300. For all vessels, the deformable model was applied to both the common carotid-to-internal carotid and to the common carotid-to-external carotid. The surfaces from both were superimposed for visualization.

For two cases where stenosis of the internal carotid artery occurred, it was necessary to add an anchor point at the groove between the internal and external carotid arteries to obtain an accurate surface reconstruction (location is shown in figure 6). Errors otherwise occurred at this location due to poor edge quality and the interference of the external carotid artery in the continuity of the cylindrical vessel surface. Otherwise, the degree of stenosis observed in the reconstructed surfaces was nearly that determined from the source and MIP images in the two vessels. (20% stenosis in model vs. 20-39% stenosis measured from MIP, 45% stenosis in model vs. 45-50% stenosis measured from MIP) Normal vessels showed no signs of stenosis but in two cases the model of the internal carotid mistakenly included a section of the external carotid where the two vessels nearly overlap. This problem could be removed by increasing the elasticity constant K_2 to $6 \times 10^4 \text{ cm}^{-1}$.

The result on one artery where significant stenosis is evident is shown in figure 6.

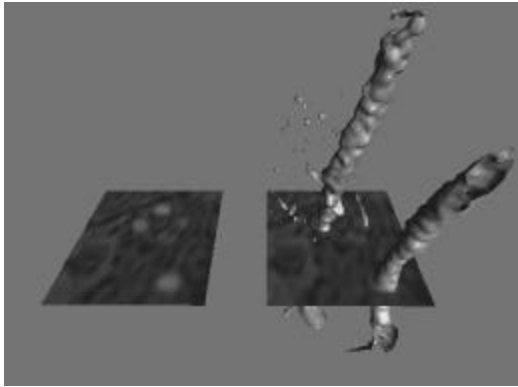


Figure5. Identifying points along the axis of the vessel. A cropped portion of the carotid MRA is shown by itself and with a 3D isosurface (right) to provide anatomical context which helps to follow a given vessel from one axial slice to another.

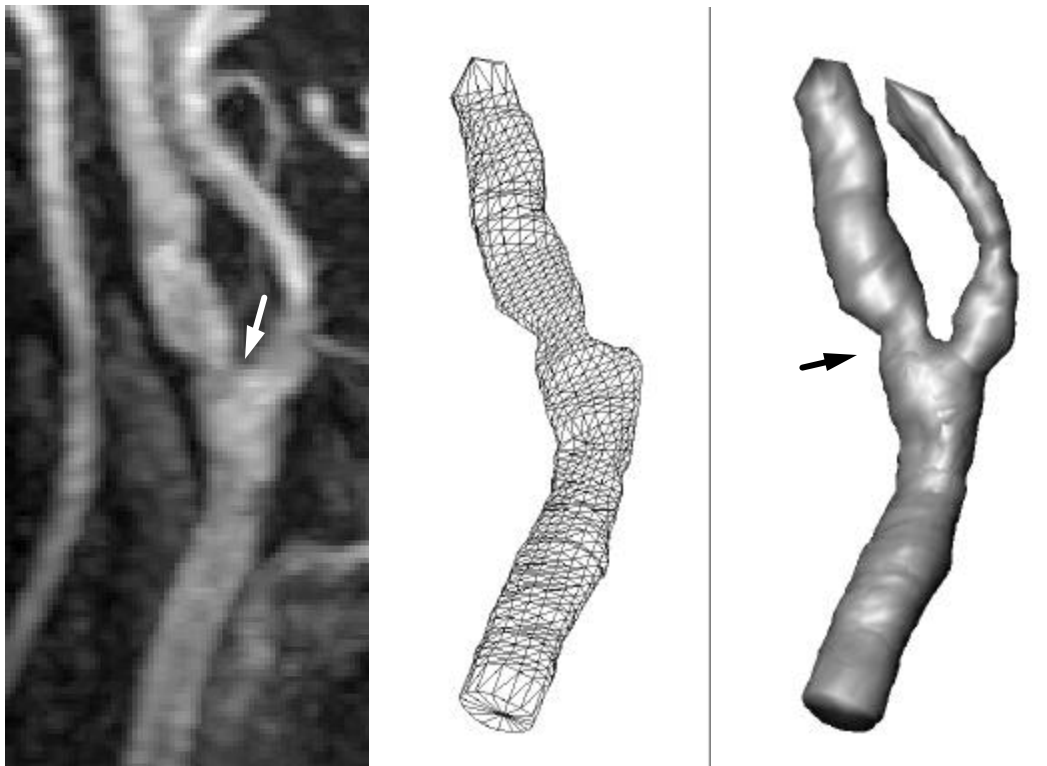


Figure 6. Surface reconstruction of carotid artery with stenosis (black arrow). Image is shown as maximum intensity projection of cropped region from sagittal view (left), as 3D surface from deformable model of both internal and external carotid arteries (right) and as wireframe mesh (left)(only internal and common carotid artery shown in wireframe view). In addition to identifying points along the vessel axis, the user also indicated a point at the groove between the internal and external carotid arteries (white arrow).

5. Measurement of Stenosis

Stenosis of the carotid artery is conventionally measured from a 2D projection image. The standard definition of the degree of stenosis is based on the comparison of the vessel diameter at the stenosed location with the normal vessel diameter usually measured at a downstream location^{1,15}. Of course, in this measurement, the projection angle may be important due to orientation effects so a variety of projections are obtained and the stenosis measurement is made from the projection where the degree of stenosis is most severe. This method of stenosis measurement could also be applied to vessel surfaces but a 3D method is preferable since any given projection contains only limited information of the 3D shape. We propose a new definition of vessel diameter which is consistent with the conventional projection-based diameter measurement for convex vessel cross-sections and we provide methods for making this measurement.

We define the vessel diameter at any point along the vessel to be that of the largest sphere which can fit entirely within the vessel at that point. This is comparable to the measurement of diameter in 2D projection images which amounts to measuring the diameter of the largest circle which can fit in the vessel at a given point. This is shown in figure 7.

Determination of the maximal spheres from a surface mesh of the vessel requires several steps. The first step is to convert the surface mesh to a high-resolution binary mask. This conversion is done by finding all points within the high-resolution image which intersect with any of the surface triangles to produce a shell in the binary image in which all points on the boundary are turned on. A region-growing operation is then carried out such that all points within the vessel are also turned on.

The second step in measuring vessel diameter is skeletonization of the binary mask. A variety of skeletonization algorithms have been proposed for 2D and 3D binary images^{16,17,18,19} but the most appropriate for this application is the Ordered-Region Growing (ORG) skeletonization algorithm²⁰. The ORG skeletonization will the largest sphere which can pass within the vessel between any two given points. Thus if two points are specified to either side of the stenosis region, the maximal sphere which can pass through the stenosis will be obtained. The skeletonization proceeds as follows. First, the binary mask is transformed to a distance map in which the intensity at each point is the distance from that point to the nearest point outside of the vessel. A growth process is initiated from one of the seed points, s_0 . A growth process then occurs in which growth proceeds from the single point on the boundary of the growing region, B_n which has the highest intensity or in this case the greatest distance value. This process is repeated until the second seed point is reached. Formally, $I: \mathbb{R}^N \rightarrow \mathbb{R}$ is the image intensity and Neighbors is the set of neighbors of any given point in the image. W_n is the set of points within the grown region at any iteration.

$$s_n = \text{Max}(B_n) = \{x \in B_n \mid \forall y \in B_n, I(x) \geq I(y)\} \quad (6)$$

$$G_n = \text{Neighbor}(s_n) \setminus W_n \quad (7)$$

$$B_{n+1} = (B_n \cup G_n) \setminus s_n \quad (8)$$

The skeleton of the vessel is then the path of the growth from the start seed point to the end seed point. The distances at each point along the vessel skeleton are then the vessel radii at those points.

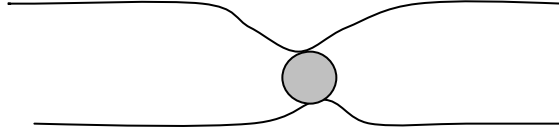


Figure 7. Measurement of the minimum diameter of vessel in a projection image is equivalent to determining the largest circle which can pass through a vessel (Profile of vessel shown in darker lines). This concept can be extended to 3D by determining the largest sphere which can traverse the vessel within the 3D boundaries of the vessel.

6. Conclusions

Images of the carotid artery lumen can now be obtained non-invasively and in 3D with MRA. However, quantification of shape from these images is challenging due to image noise and artifacts. We have presented, in this paper, a semi-automated method for reconstructing the surface of the carotid artery and a method for characterizing the lumen shape. These methods are straightforward and require only the input from the user of a limited number of points along the central axis of the vessel and a single point in the groove where the internal and external carotids join. Unlike a previous deformable model of the carotid artery, exact determination of the vessel axis is not important and the model has no known bias towards producing smaller or larger diameter vessels. Further testing of the method will be carried out including comparison with x-ray angiography.

4. References

- ¹ North American Symptomatic Carotid Trial (NASCET) Steering Committee, "North American symptomatic carotid endarterectomy trial; methods, patient characteristics and progress," *Stroke*, 22:711-720, 1991
- ² R.L. Vanninen, H.I. Manninen, P.K. Partanen, H. Tulla, P.A. Vainio, "How should we estimate carotid stenosis using magnetic resonance angiography?", *Neuroradiology*, 38: 299-305, 1996
- ³ B.A. Wasserman, E.M Haacke, D. Li, "Carotid plaque formation and its evaluation with angiography, ultrasound, and MR angiography," *JMRI*, 4:515-527, 1994
- ⁴ J.S. Milner, J.A. Moore, B.K. Rutt, D.A. Steinman, "Hemodynamics of human artery bifurcations: computational studies with models reconstructed from magnetic resonance imaging of normal subjects," *J. Vasc. Surg.*, 27: 143-156, 1998

-
- ⁵ J.A. Moore, D.A. Steinman, D.W. Holdsworth, "Accuracy of computational hemodynamics in complex arterial geometries reconstructed from magnetic resonance imaging," *Ann Biomed Eng.*, 27: 32-41, 1999
- ⁶ H.E. Cline, W.E. Lorensen, S.P. Souza, F.A. Jolesz, R. Kikinis, G. Gerig, T.E. Kennedy, "3D surface rendered MR images of the brain and its vasculature," *JCAT*, 15:344-351, 1991
- ⁷ D.L. Wilson, J.A. Noble, "Segmentation of cerebral vessels and aneurysms from MR angiography data," *Lecture Notes in Computer Science*, 1230:423-428, 1997
- ⁸ T. Lei, J.K. Udupa, P.K. Saha, D. Odhner, "MR angiographic visualization and artery-vein separation," *Proc. SPIE*, 3658:58-66, 1999
- ⁹ P.J. Yim, D. Kim, and C. Lucas, "High Resolution Four-dimensional surface reconstruction of the right heart and pulmonary arteries," *Proc. SPIE, Medical Imaging*, 3338:726-738, 1998
- ¹⁰ P.J. Yim, R.M. Summers, "Analytic surface reconstruction by local threshold estimation in the case of simple intensity contrasts," *Proc. SPIE, Medical Imaging*, 3660:288-300, 1999
- ¹¹ T. McInerney, D. Terzopoulos, "Medical image segmentation using topologically adaptable surfaces," *Proc. CVRMed '97, Grenoble, France, March*, 1997.
- ¹² A.J. Bulpitt, E. Berry, "Spiral CT of abdominal aneurysms: comparison of segmentation with an automatic 3D deformable model and interactive segmentation," *Proc. SPIE, Medical Imaging*, 3338:938-46, 1998
- ¹³ S. Aylward, E. Bullitt, S. Pizer, D. Eberly, "Intensity ridge and widths for tubular object segmentation and description," *Proc. of IEEE Workshop, Mathematical Methods in Biomedical Image Analysis*, June, 1996
- ¹⁴ A.F. Frangi, W.J. Niessen, R. M. Hoogeveen, "Model-based quantitation of 3-D magnetic resonance angiographic images," *IEEE T. Med. Imaging*, 18:946-956, 1999
- ¹⁵ R.L. Vanninen, H.I. Manninen, P.K. Partanen, H. Tulla, P.A. Vainio, "How should we estimate carotid stenosis using magnetic resonance angiography?", *Neuroradiology*, 38:299-305, 1996
- ¹⁶ S.W. Lee, L. Lam, C.Y. Suen, "A systematic evaluation of skeletonization algorithms," *International Journal of Pattern Recognition and Artificial Intelligence*, 7: 239-261, 1993
- ¹⁷ P.K. Saha, B.B. Chaudhuri, D.D. Majumder, "A new shape preserving parallel thinning algorithm for 3D digital images," *Pattern Recognition*, 30:1939-1955, 1997
- ¹⁸ T.-C. Lee, R.L. Kashyap, C.-N. Chu, "Building skeleton models via 3-D medial surface/axis thinning algorithms," *CVGIP: Graphical Models and Image Processing*, 56:462-478, 1994
- ¹⁹ I. Nystrom, "Skeletonization applied to magnetic resonance angiography images," *Proc. of SPIE*, 3338:693-701, 1998
- ²⁰ P.J. Yim, D. Kim, R.M. Summers, "A path-wise definition of the watershed line and a watershed-like skeletonization," *In submission*